Crystallization Kinetics and Morphology Control of Formamidinium–Cesium Mixed-Cation Lead Mixed-Halide Perovskite via Tunability of the Colloidal Precursor Solution

David P. McMeekin, Zhiping Wang, Waqaas Rehman, Federico Pulvirenti, Jay B. Patel, Nakita K. Noel, Michael B. Johnston, Seth R. Marder, Laura M. Herz, and Henry J. Snaith*

The meteoric rise of the field of perovskite solar cells has been fueled by the ease with which a wide range of high-quality materials can be fabricated via simple solution processing methods. However, to date, little effort has been devoted to understanding the precursor solutions, and the role of additives such as hydrohalic acids upon film crystallization and final optoelectronic quality. Here, a direct link between the colloids concentration present in the $[HC(NH_2)_2]_{0.83}Cs_{0.17}Pb(Br_{0.2}I_{0.8})_3$ precursor solution and the nucleation and growth stages of the thin film formation is established. Using dynamic light scattering analysis, the dissolution of colloids over a time span triggered by the addition of hydrohalic acids is monitored. These colloids appear to provide nucleation sites for the perovskite crystallization, which critically impacts morphology, crystal quality, and optoelectronic properties. Via 2D X-ray diffraction, highly ordered and textured crystals for films prepared from solutions with lower colloidal concentrations are observed. This increase in material quality allows for a reduction in microstrain along with a twofold increase in charge-carrier mobilities leading to values exceeding 20 cm² V⁻¹ s⁻¹. Using a solution with an optimized colloidal concentration, devices that reach current–voltage measured power conversion efficiency of 18.8% and stabilized efficiency of 17.9% are fabricated.

In recent years, metal halide perovskite solar cells have gained tremendous attention, reaching certified efficiencies of 22.1% power conversion efficiency.[1] This rapid success is partly due to a versatile solution-based fabrication process which allows for a wide range of deposition techniques such as: spin-coating,[2,3] two-step interdiffusion,[4] dip-coating,[4] inkjet printing,[5,6] and spray pyrolysis.[7] These solution-based fabrication methods of perovskite films have been used in a variety of devices ranging from field-effect transistors,[8] light-emitting devices (LED),[9] photodetectors,[10,11] to solar cells.[2–4,12] Although most perovskite thin films are fabricated using a salt-based precursor solution, little effort has been dedicated to characterizing the structure and time-dependent evolution of the species present in solution and the impact this has on the quality of the resulting films. Furthermore, it has been shown that additives to the precursor solution can impact the nucleation rate, morphology, grain size, and crystallinity of the perovskite. Additives, such as polymers,[13] small molecules,[14,15] metal ions,[16] water,[17] or acids,[18–24] can play a vital role in material quality, enabling improvements in material stability, optoelectronic properties, and photovoltaic performance.

Work by Yan et al. characterized the 1:1 $CH_3NH_3I:PbI_2$ stoichiometric precursor solution as a colloidal dispersion in a mother solution, rather than a pure solution.[25] When fabricated on planar substrate, this colloidal solution forms films with poor morphology, due to the presence of rod-shaped colloids comprised of a soft coordination complex in the form of a lead polyhalide framework.[25] The authors show that the colloid distribution can be tuned by varying the organic to inorganic compound ratio in the precursor solution, using excess CH_3NH_3I (MAI) and CH_3NH_3Cl (MACl). However, the authors were unable to remove the 1D PbI_2 rod-like structures in the widely used stoichiometric 1:1 precursor solution. Adding excess organic cation to dissolve these colloids may be incompatible with recently published mixed-cation perovskites that contain both organic and inorganic cations,[26–29] since this will alter the precise $[HC(NH_2)_2]^+$ (formamidinium, FA) to Cs ratio, which is required to form the appropriate perovskite composition. In addition, FAI has a lower effective volatility than MACl, for instance, and hence excess quantities will not be so readily removed. Herein, we address this problem by utilizing acidic additives to trigger the dissolution of the

D. P. McMeekin, Dr. Z. Wang, W. Rehman, J. B. Patel, Dr. N. K. Noel, Prof. M. B. Johnston, Prof. L. M. Herz, Prof. H. J. Snaith
Clarendon Laboratory
University of Oxford
Parks Road, Oxford OX1 3PU, UK
E-mail: henry.snaith@physics.ox.ac.uk
F. Pulvirenti, Prof. S. R. Marder
School of Chemistry and Biochemistry
Georgia Institute of Technology
901 Atlantic Drive, Atlanta, GA 30332-0400, USA

**ADVANCED
SCIENCE NEWS**
www.advancedsciencenews.com

**ADVANCED
MATERIALS**
www.advmat.de

colloids in the precursor solution. However, after the initial incorporation of the acid, full dissolution of the colloids occurs over a period of tens to hundreds of hours. We show that with a fixed concentration of additional hydrohalic acids, we can transition from a colloidal solution to one without any large colloids by simply using time as a varying parameter, thus decoupling the observed effects from additional coordination of halide ions, as recently reported by Pan et al.[22] We show that during this time period, the colloids in suspension gradually dissolve, critically impacting the crystallization kinetics of the thin films. Thus, we show that the colloidal concentration in the precursor solutions plays a significant role in determining the variations in morphology, crystallinity, texture, and optoelectronic properties of the perovskite.

In this work, we focus on the role of hydrohalic acids, specifically hydroiodic (HI) and hydrobromic (HBr), as additives, when incorporated into the mixed-cation lead mixed-halide $FA_{0.83}Cs_{0.17}Pb(Br_{0.2}I_{0.8})_3$ perovskite precursor solution. Although hydrohalic acids have previously been used as additive to precursor solutions to create smoother films, improve their surface coverage,[18,22] alter crystal structure,[21] and even reduce the onset temperature of crystallization of the all-inorganic $CsPbI_3$ perovskite,[30] there is still little understanding of what is driving this behavior. Here, using dynamic light scattering (DLS), we link the effect of an acid additive to the dissolution of the lead polyhalide colloidal framework. We show that by dissolving the colloids over a given time period, we can substantially change the nucleation and growth dynamics and hence, the final film morphology of the mixed-cation lead mixed-halide perovskite system. In turn, film quality is improved by increasing grain size, crystallinity, and charge-carrier mobilities. However, we observe a trade-off between morphology and crystal quality, where films with the largest grain size are prone to pinhole formation. Recently, it has been shown that improvements in crystallinity and larger grain sizes can impact the stability of the perovskite thin film.[31,32] Using a precursor solution with an optimized colloidal distribution, we fabricated planar heterojunction n-i-p perovskite solar cells, demonstrating current–voltage determined power conversion efficiencies of over 18.8%, and a stabilized efficiency of 17.9%.

Morphology plays a key role in the device performance of perovskite solar cells. Poor morphology can lead to the creation of voids in the perovskite thin film, which will reduce the surface coverage of the light-absorbing layer, thus reducing the short-circuit (J_{SC}) of the device. More importantly, the pinholes will also result in an undesirable contact between the electron and hole selective charge extraction layers. This contact area between the n and p-type layers creates paths of low resistance within the solar cell, thus reducing the shunt resistance (R_{SH}), and ultimately reducing the open circuit voltage (V_{OC}) and fill factor (FF) of the device. Here, we present a simple and effective
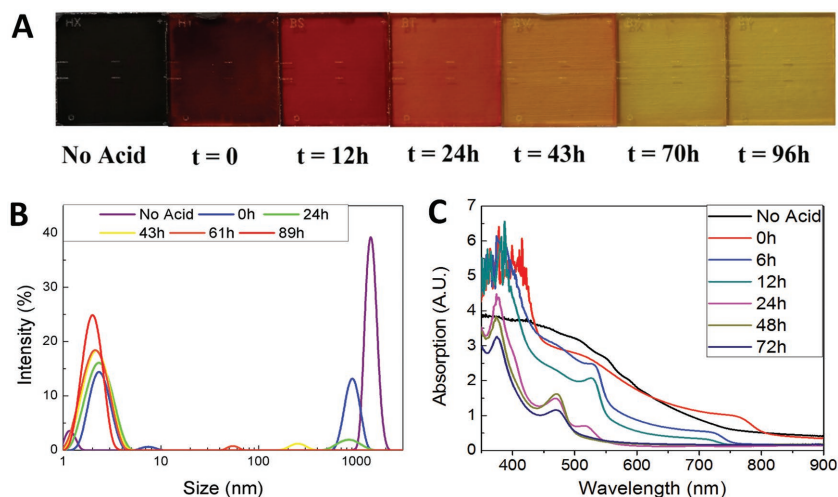

Figure 1. Impact of colloids in the precursor solution on the nucleation stage of the $FA_{0.83}Cs_{0.17}Pb(Br_{0.2}I_{0.8})_3$ perovskite system. A) A series of photographs of thin films spin-coated and dried at 70 °C under nitrogen, prepared with solutions aged in an N_2 atmosphere for various periods of time after the addition of hydrohalic acid. B) Colloidal hydrodynamic size distribution via dynamic light scattering of various perovskite solutions. C) Ultraviolet–visible absorbance spectra of corresponding thin films.

method of controlling the morphology of the mixed-cation lead mixed-halide perovskite by tuning the density of colloids found in the precursor solution. We suggest that these lead polyhalide colloids, identified as $[PbX_3]^{-1}$, $[PbX_4]^{-2}$, $[PbX_5]^{-3}$, $[PbX_6]^{-4}$ by Yan et al.,[25] serve as nucleation centers in the formation of perovskite thin films.

We first show that tuning the distribution of the various colloids within the precursor solution impacts the crystallization kinetics of the perovskite. We first investigate if the addition of hydroiodic (HI) and hydrobromic (HBr) acids to the perovskite precursor solution has an impact upon the colloids in the solution. Our precursor solution is composed of CsI, FAI, $PbBr_2$, and PbI_2 in order to obtain a molar ratio of FA:Cs:Br:I of 0.83:0.17:0.2:0.8 in DMF (N,N-dimethylformamide) at a 1.15 molar concentration. To this solution we added HI and HBr to obtain a halogen molar ratio of 8:2, resulting in the addition of a volume concentration of 81.7 $\mu L\ mL^{-1}$ of HI (57 wt% in H_2O) and 17.6 $\mu L\ mL^{-1}$ of HBr (48 wt% in H_2O). In **Figure 1**A, we show photographs of films coated from precursor solutions with various aging times after the addition of the acid, after spin-coating and a low-temperature 70 °C drying step in a nitrogen atmosphere. We observe a noticeable color change, from black to yellow, as a function of time after addition of the acids. For solutions without an acidic additive, the films turn dark during the spin-coating process, prior to the 70 °C drying step, whereas with hydrohalic acid, the as-spun films only show a slight color change. We note that this behavior is also observed for films prepared with hydrohalic acids without hypophosphorous acid (HPA), a reducing agent used as a stabilizer in commercial HI solution (Figure S1, Supporting Information). In Figure 1B, we show the DLS intensity distribution of these precursor solutions after the initial addition of the acid. Over the course of time, we see the disappearance of the large hydrodynamic micrometer-sizes particle distribution. In Figure 1C, we show the ultraviolet–visible (UV–vis) absorbance spectra of the

**ADVANCED
SCIENCE NEWS**
www.advancedsciencenews.com

**ADVANCED
MATERIALS**
www.advmat.de

corresponding 70 °C dried thin film. We observe the gradual disappearance of the black perovskite absorption onset.

The colloids that are initially present in the stoichiometric $FA_{0.83}Cs_{0.17}Pb(Br_{0.2}I_{0.8})_3$ perovskite precursor solution appear to slowly dissolve over the course of days after the addition of the hydrohalic acids. After the addition of the acids, a noticeable increase in solubility can be seen with the naked eye, where the solution loses its opaque or "cloudy" appearance and becomes a translucent yellow solution. Nevertheless, these clear solutions still display a Tyndall effect (light scattering). It has been reported that the measured DLS intensity relates to rod-shaped colloids.[25] As we show in Figure S2 (Supporting Information), we observe the presence of these nanorods in unheated thin films prepared with an acid-free solution, consistent with observations made by Yan et al. and Bi et al.[25,33] Perovskite films fabricated from a solution with a high concentration of colloids quickly turn dark in the process of spin-coating, while film spun with "colloid-free" solutions remained yellow. Notably, we observe similar time-dependence behavior for "cesium-free" $FAPb(Br_{0.2}I_{0.8})_3$ and "formamidinium-free" $CsPb(Br_{0.2}I_{0.8})_3$ precursor solutions, suggesting that the colloids are lead polyhalide colloids (Figure S3, Supporting Information). The colloid concentration in the precursor solution can be tuned using two methods: by timing the addition of the acid additives, as we show in Figure 1, or simply by mixing a fully aged "colloid-free" solution with a fresh colloidal solution, immediately prior to spin-coating, as we show in Figure S4 (Supporting Information). We note that at 70 °C in an N_2 atmosphere, the colloid-free films retain their yellow colors for an extended period of

time, as we show in Figure S5 (Supporting Information). We also note that the hydrohalic acids have considerable amount of water, ranging from 48 wt% for HBr to 57 wt% for HI. However, as we show in Figure S6 (Supporting Information), the addition of water did not contribute to significant colloid dissolution. Furthermore, as we show in Figure S7 (Supporting Information), we observe a decrease in scattering behavior of the precursor solution, along with a delay in perovskite nucleation, and an increase in grain sizes for films prepared with HPA as additive, a nonhalogenated acid, while the addition of iodine and bromine do not result in a nucleation delay or larger grain sizes. Although the addition of HPA leads to poor film morphology for the $FA_{0.83}Cs_{0.17}Pb(Br_{0.2}I_{0.8})_3$ perovskite system, this result points toward the proton being the active component in hydrohalic acids, rather than the halide anions.

We now focus on our investigation of the subsequent high-temperature annealed perovskite films, during crystallization, in more detail. In **Figure 2**, we show optical microscopy images of the films during their annealing process. We show the full video for each concentration in Video S1 (Supporting Information). Although in most films we cannot resolve individual perovskite crystallites and/or nucleation centers in the optical microscopy image, we interpret these images to indicate that the density of nucleation sites for crystal growth is reduced, as the solution aging time after acid addition is increased. After the first nucleation stage, a subsequent stage follows where crystal growth occurs. Already in the $t = 0$ s films, there may have been some degree of growth that is resulting in the red/brown coloration of the films due to the low-temperature 70 °C
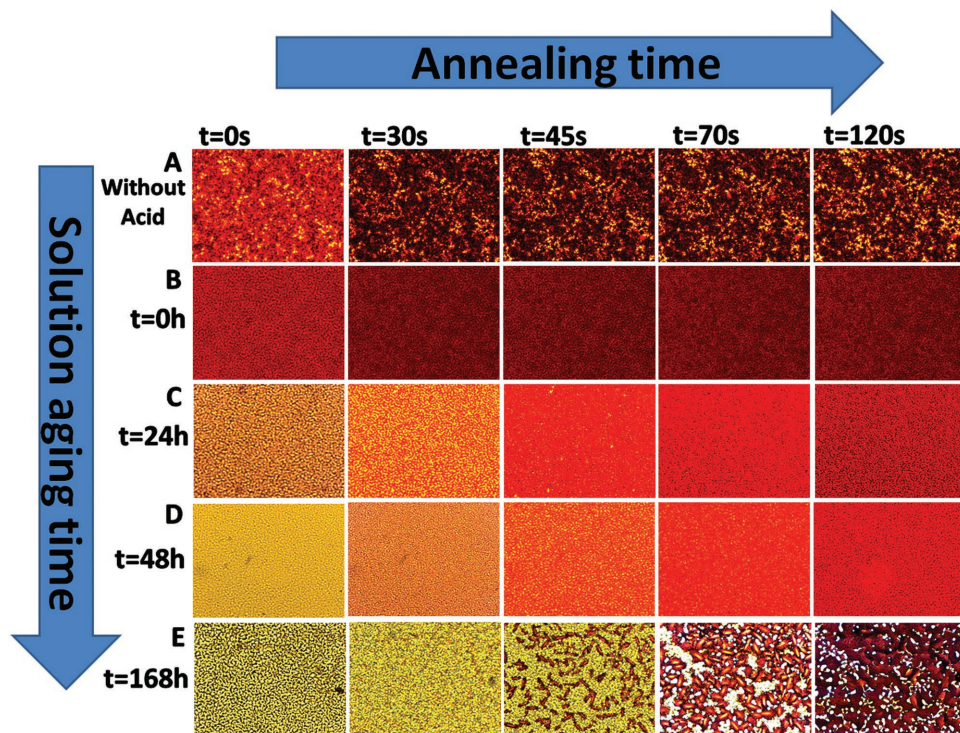

Figure 2. Growth kinetics of the $FA_{0.83}Cs_{0.17}Pb(Br_{0.2}I_{0.8})_3$ perovskite system with various colloid concentrations. Microscopy images using a 50× magnification of postnucleation thin films heated at 220 °C in an air atmosphere; prepared using precursor solutions aged with an acid for a period of time. A–E) Precursor solution aged for 0 h without hydrohalic acids (A), 0 h with the addition of acids (B), 24 (C), 48 (D), and 168 h (E).

drying step. However, for full crystallization, a high-temperature heating process converts all colored films into the black perovskite phase. Furthermore, we observe that solutions with higher colloidal concentrations result in short growth periods, where crystal growth has already largely occurred during the 70 °C drying step, and remains relatively unchanged during the high-temperature (Figure 2A) anneal. However, solutions with lower colloidal concentrations allow for a longer crystal growth, where the black perovskite phase appears later into the crystal growth period (Figure 2C–E). Figure 2A–D shows a dense and uniform distribution of growing crystals, resulting in impingement of the grains against one another during the growth stage and providing a full surface coverage. Although Figure 2E does not provide full surface coverage, we observe at $t = 45$ s the initial growth of the black perovskite phase crystals, originating from individual seeds. In addition, we show in Figure S8 (Supporting Information), a series of photographs showing the variation in crystallization rate with respect to the precursor solution.

We now appear to have sufficient information to provide a hypothesis about the impact of the addition of the acids, and the presence of the colloids upon thin film crystallization. The nucleation and growth characteristics of perovskite crystals are both affected by the amount and size of nuclei located in the precursor solution. We propose that the large colloids, inherently present in the $FA_{0.83}Cs_{0.17}Pb(Br_{0.2}I_{0.8})_3$ perovskite precursor solution, act as nucleation sites to initiate the perovskite formation. Thin films prepared with solutions with high scattering light behavior caused by the colloids undergo rapid perovskite crystallization due to the higher nucleation site density, while films prepared with precursor solutions that have little to no colloids lead to a prolonged crystal growth period due to fewer nucleation sites.

From classical nucleation theory, we know that nucleation can occur in a heterogeneous or a homogeneous manner.[34] In the case of perovskite thin films, nucleation occurs on foreign surfaces and/or via nuclei; thus, heterogeneous nucleation is likely to be the dominant nucleation mechanism. The impact of surface energy on morphology, using n and p-type layers with various wetting properties, has been discussed by Bi et al.[35] However, the free energy barrier for nucleation can also be lowered with the introduction, or existence of nuclei in the perovskite solution. Let us consider a simplified case of heterogeneous nucleation where a solid, spherically shaped nucleus, immersed in a liquid, is located on a solid surface. The free energy needed for heterogeneous nucleation relates to the corresponding free energy change associated with its homogeneous nucleation multiplied by a factor relating to interfacial tensions γ.[36–38] Since this factor is less than unity, heterogeneous systems have a lower free energy change than homogeneous systems, and thus a lower nucleation barrier:

$$G_{Heterogeneous} = G_{Homogeneous} \frac{(2+\cos\theta)(1-\cos\theta)^2}{4}$$ (1)

where θ is the contact angle between the crystalline deposit and the foreign solid surface, corresponding to a wetting angle.

Here, by controlling the concentration of lead polyhalide colloidal dispersion in the precursor solution, we are effectively tuning the interfacial tensions γ between the liquid solution,

solid colloid, and substrate, thus varying the amount of preferential sites where heterogeneous nucleation occurs. Therefore, even if the colloids are lead polyhalide colloids and not perovskite colloids, we postulate that the colloids offer preferential sites for heterogeneous nucleation and are thus acting as nucleation sites during the crystallization. Incidentally, with few heterogeneous nucleation sites, polycrystalline film growth occurs so sparsely that the growing domains do not fully impinge upon each other, and nonuniform films with pinholes are produced.

In **Figure 3**, we show the impact of the colloidal concentration on the morphology, grain size, and crystallinity of the perovskite films. In Figure 3A–E, we show the scanning electron microcopy (SEM) image of the perovskite films deposited using various precursor solutions on fluorinated tin oxide (FTO) substrates. The use of an "acid-free" perovskite solution results in a thin film with significant amounts of pinholes and intergranular cracking. The addition of the acids, which triggers the dissolution of the colloids over, allows for the growth to commence after spinning of the sample. Figure 3A–D shows the increase in grain size from ≈100 nm without the addition of the acids to several micrometers for colloid-free solutions under identical annealing conditions. Figure 3E shows the formation of cube-like crystal grains with distinguishable facets when annealed at a higher temperature, illustrating the compromise between grain size and morphology.

By reducing the density of nucleation sites, we can obtain larger polycrystalline grain domains with a preferred orientation. However, we observe a distinct trade-off between the grain sizes and pinhole density. Since crystal growth not only occurs in the lateral direction but also in the vertical direction, the formation of grains above 10 μm in size tends to be accompanied with undesirable pinholes. Hence, the optimal precursor solution is one that contains a proper colloids concentration in order to provide a pinhole-free film with as large grain morphology as possible. However, it is important to note that this ideal balance depends on the surface energy and roughness of the n or p-type coated substrate. Therefore, the colloidal distribution of the precursor solution can be adjusted for optimum morphology depending on the hydrophobicity of the electron or hole accepting layer that the perovskite will crystallize upon.

In order to understand the impact of this control of thin film growth upon the crystalline quality of the material, we analyze the material quality using 2D X-ray diffraction (XRD^2). By employing image plates or a 2D charged-couple device (CCD) array as detector, this allows us to measure complete Debye–Scherrer cones simultaneously. In contrast to a conventional 1D XRD diffraction profile, we can directly observe the effects of grain size and texture from the 2D diffraction profile. In Figure 3F, we show a series of 2D diffraction patterns of thin films prepared using various precursor solutions. To perform a quantitative analysis, we integrate the intensity along the azimuthal angle over the diffraction pattern arising from the (100) planes that form a Debye–Scherrer ring at ≈1 Å^{-1}, as we show in Figure 3F,G. We observe that thin films prepared from solutions with high colloid concentrations result in little preference of orientation, where samples exhibited diffraction rings with intensities along the entire arc segment, indicative of fewer crystal domains with preferential orientations. From Figure 3G, we observe three preferential orientations in the orientation
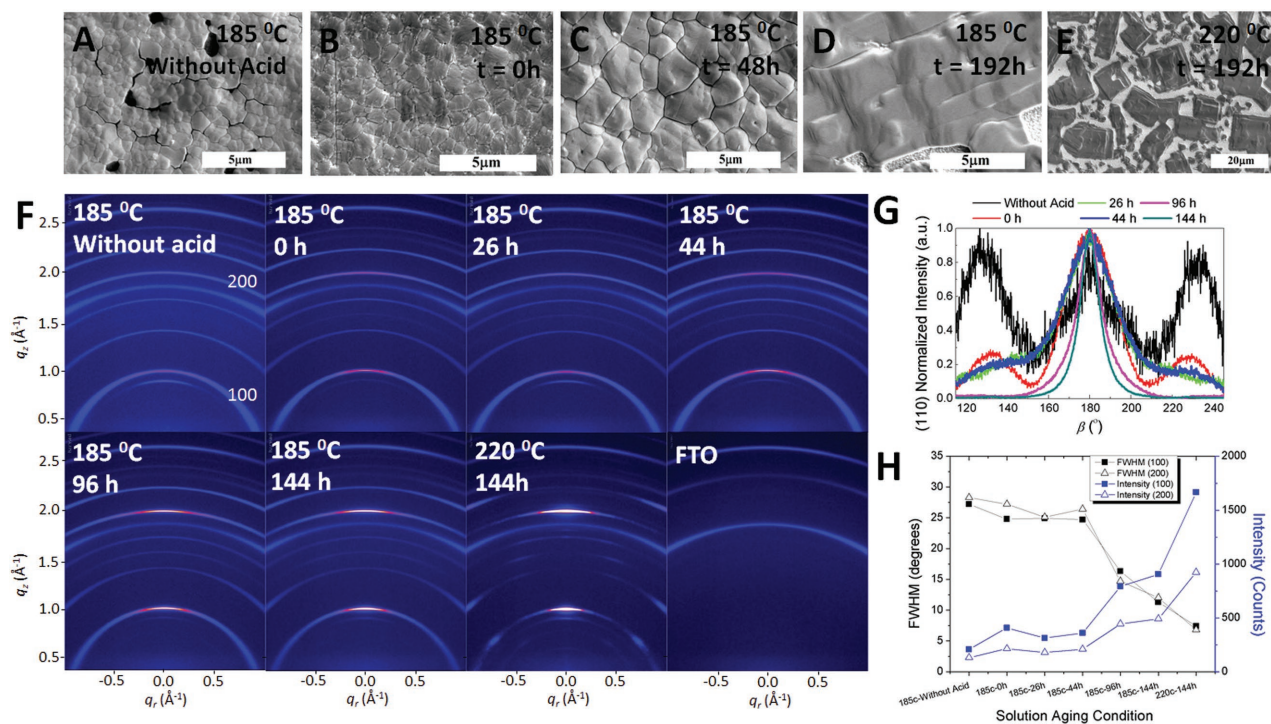
1607039 (4 of 8)

**ADVANCED
SCIENCE NEWS**

www.advancedsciencenews.com

**ADVANCED
MATERIALS**

www.advmat.de

Figure 3. Impact of colloids in the precursor solution on morphology and crystal quality. A–E) A series of top-view scanning electron microscope (SEM) images of a fully annealed $FA_{0.83}Cs_{0.17}Pb(Br_{0.2}I_{0.8})_3$ perovskite thin film prepared with/and without hydrohalic acids, where the solutions were aged for various time periods. F) A series of 2D X-ray diffraction patterns of corresponding thin film after full annealing step. G) Normalized (100) diffraction peak of corresponding perovskite thin film. H) Azimuthal (β) full-width half maximum (FWHM) of (100) and (200) orientation, along with the peak intensity of the (100) and (200) diffraction peak.

distribution, which are located at $\beta = 180°$, $127°$, and $233°$. Apart from the $\beta = 180°$ peak, the origin of the other two peaks can be attributed to the corners of cube-shaped crystallites. Nevertheless, all these peaks exhibit large full-width half maximum (FWHM) values, as we show in Figure 3H, indicating the poor film crystallinity for thin films prepared with large amount of colloids (i.e., without an acid additive). In contrast, we observed significant texturing for thin films prepared from solutions with low amount of colloids. Due to the extended growth period, these thin films exhibit discrete Bragg spots along the identical diffraction ring, indicative of crystal domain orientation. The texturing trend, which we see in the XRD^2, coincides with the trend seen in grain sizes we observe via SEM. Films prepared with a colloid-free solution and annealed at high temperature, result in XRD^2 diffraction patterns approaching single crystalline quality.

We further assess the impact of the colloids on crystal quality by conducting a local strain (microstrain) analysis. Different nucleation and crystal growth kinetics of perovskite thin films can be responsible for variations in microstrain. These small fluctuations in the lattice spacing are induced by the presence of crystal imperfections/structural defects including dislocations, vacancies, and stacking faults.[39–41] Here, we quantify the effects of microstrain in our perovskite films by analyzing the peak broadening in the diffraction patterns according to the modified Williamson–Hall method.[16,40,42,43] Additional information is provided in the Supporting Information. We show in **Figure 4**A, a clear reduction in microstrain as we dissolve the colloids in

the precursor solution. This allows for a slower crystal growth, minimizing the localized strain within the structure.

In order to characterize the charge-carrier mobility in the fully crystallized films, we performed optical-pump terahertz-probe (OPTP) spectroscopy. In Figure 4B, we show charge-carrier mobility of the $FA_{0.83}Cs_{0.17}Pb(Br_{0.2}I_{0.8})_3$ perovskite for thin films fabricated with different precursor solutions. We measure more than a twofold increase in charge-carrier mobilities for films processed from solutions with fewer amounts of colloids, from <10 to >20 $cm^2\ V^{-1}\ s^{-1}$. This coincides with the increase in crystallinity and texturing observed in the XRD^2 diffraction patterns and the reduction in microstrain.

We make a specific note about microstrain: microstrain is not a property that is often employed when analyzing perovskite absorbers within the perovskite research community. However, recently several studies, using different perovskite systems, have shown a good correlation between reduced microstrain and enhanced optoelectronic properties.[16,43,44] We suggest that either microstrain itself, or the crystal defects responsible for microstrain, or both are closely related to the defects responsible for negating high optoelectronic quality in these materials. Hence, with respect to attempting to realize an ideal perovskite semiconductor, minimizing microstrain in the polycrystalline thin films is likely to be a good metric to assess, and lead to improved optoelectronic quality.

In order to investigate the impact of the differing films in complete solar cells, we fabricated a series of planar heterojunction solar cells using precursor solutions with various colloidal
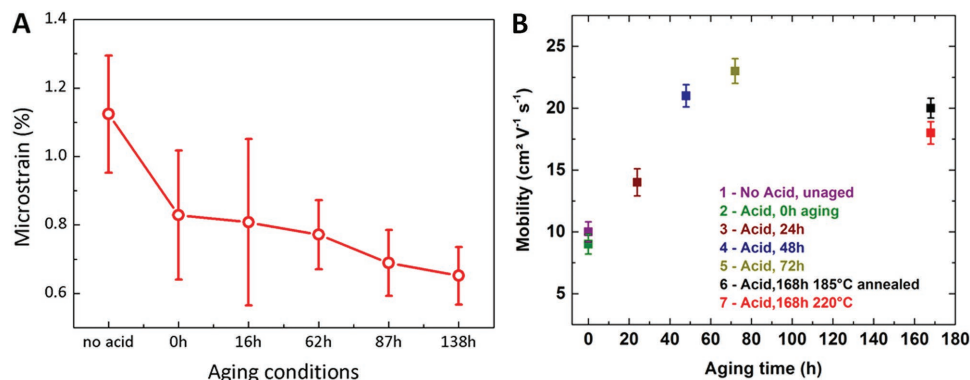
1607039 (5 of 8)

Figure 4. Impact of colloids on crystal lattice and optoelectronics properties. A) Calculated microstrain derived from XRD pattern of samples with different precursor solution aging conditions. The error bars for each concentration in the plot are determined from the fits in Figure S9 (Supporting Information). B) The effective charge-carrier mobilities, corrected for surface coverage, of a range of perovskite films prepared with precursor solution with various concentrations of colloids. Error bars indicate the range of values obtained.

concentrations, the results of which we show in **Figure 5**A. We show the device architecture in Figure 5B, consisting of PCBCB [phenyl-C61-butyric acid benzocyclobutene ester], a crosslinkable fullerene derivative,[45,46] acting as the electron-selective layer, $FA_{0.83}Cs_{0.17}Pb(I_{0.8}Br_{0.2})_3$ as perovskite absorber, and Li-TFSI–doped [TFSI, bis(trifluoromethanesulfonyl)imide]

spiro-OMeTAD [2,2′,7,7′-tetrakis(N,N-di-p-methoxyphenylamine)-9,9′-spirobifluorene] with tBP [4-tert-butylpyridine] additive as the hole-collection layer, capped with a gold cathode. The SEM cross-section image shows a dense and continuous perovskite film with grain sizes of over 2.5 μm. The performance trend is in good accordance with morphology, grain size, crystallinity,
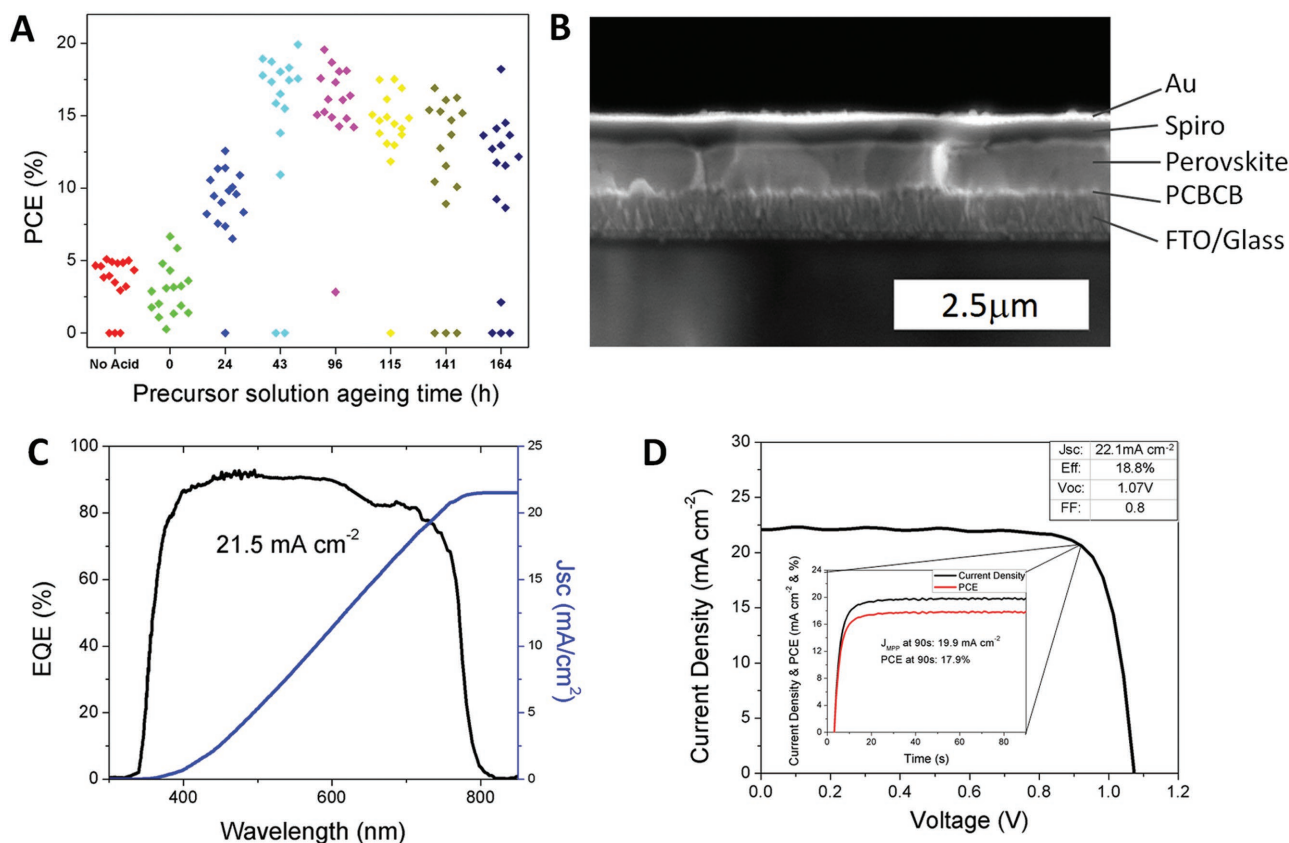

Figure 5. Impact of precursor solution aging time on solar cell device performance. A) Impact of precursor solution aging time on power conversion efficiency. B) Cross-sectional, scanning electron microscope image of a $FA_{0.83}Cs_{0.17}Pb(I_{0.8}Br_{0.2})_3$ planar heterojunction solar cell prepared with a precursor solution aged for 48 h using hydrohalic acids. C) EQE spectrum measured in short-circuit (J_{SC}) configuration and the integrated current density for the optimized perovskite solar cell. D) Forward bias to short-circuit I–V curve for the best stabilized perovskite device fabricated, measured at a 0.38 V s^{-1} scan rate. The inset figure shows the photocurrent density and power conversion efficiency measured at the maximum power point for a 90 s time span.

microstrain, and charge-carrier mobilities. We observe that the optimum device performance is obtained when the solution is aged for $\approx$2 d. We show in Figure 5C the spectral response of a representative $FA_{0.83}Cs_{0.17}Pb(I_{0.8}Br_{0.2})_3$ perovskite solar cells, which yields a current density of 21.5 mA cm^{-2}. As shown in Figure 5D, we measured current–density voltage (J–V) characteristics of one of the highest-performing devices under a simulated air mass (AM) 1.5 and 100 mW cm^{-2} of sunlight. This device generated a short-circuit current density (J_{SC}) of 22.1 mA cm^{-2}, a FF of 0.8, an open-circuit voltage (V_{OC}) of 1.07 V, and a power conversion efficiency of 18.8%. Due to the hysteretic behavior of perovskite solar cells, we performed a stabilized efficiency measurement to accurately access the performance of the device. By holding the cell at a fixed maximum power point forward-bias voltage of 0.9 V, we measured the power output over time, reaching a stabilized efficiency of 17.9% (Figure 5D). As we show in Figure S10 (Supporting Information), this solar cell architecture shows stable performance when measured in air for 30 min without any encapsulation. As we show in Figure S11 (Supporting Information), the highest scanned power conversion efficiency we measured was 20.8% using a SnO_2/PCBM (phenyl-C61-butyric acid methyl ester) n-type layer. However, the stabilized efficiency of these device with PCBM are lower than devices fabricated with a crosslinked PCBCB layer. This is likely to be due to the persistent presence of pinholes in the non-crosslinked PCBM layer, despite the potential efficiency being higher. We also show in Figure S12 (Supporting Information) a histogram of the performance of over 150 devices.

We have established a relationship between the colloid concentration of the precursor solution and the crystal quality and morphology of the perovskite thin film. Hydrohalic acids initiate the dissolution of the lead polyhalide colloids, which appear to act as nucleation sites in the as-cast thin films. We show the clear impact of colloids on the crystal nucleation and growth kinetics of the mixed-cation lead mixed-halide perovskite system. Here, we employed solution aging time as a means to control the size and dispersion of colloids in the precursor solution, which leads to a surprising increase in the grain size, crystallinity, and texture. In turn, this improvement in material quality translated in an unexpected twofold increase in charge-carrier mobility to exceed 20 cm^2 V^{-1} s^{-1} and a significant reduction in microstrain. These gains in material and optoelectronic properties lead to a substantial increase in solar cell devices efficiency, reaching power conversion efficiency of 18.8% and a stabilized efficiency of 17.9%. Further investigation is still needed to identify the mechanisms through which the colloidal dissolution occurs. In addition, it will likely prove to be advantageous to develop means to overcome the trade-off between large grains and uniform pinhole-free films.

Supporting Information

Supporting Information is available from the Wiley Online Library or from the author.

Acknowledgements

Conflict of Interest

The authors declare no conflict of interest.

Keywords

[1] National Renewable Energy Laboratory, "*NREL Efficiency Chart*," **2016**.

[2] M. M. Lee, J. Teuscher, T. Miyasaka, T. N. Murakami, H. J. Snaith, *Science* **2012**, *338*, 643.

[3] A. Kojima, K. Teshima, Y. Shirai, T. Miyasaka, *J. Am. Chem. Soc.* **2009**, *131*, 6050.

[4] J. Burschka, N. Pellet, S.-J. Moon, R. Humphry-Baker, P. Gao, M. K. Nazeeruddin, M. Grätzel, *Nature* **2013**, *499*, 316.

[5] Z. Wei, H. Chen, K. Yan, S. Yang, *Angew. Chem., Int. Ed.* **2014**, *53*, 13239.

[6] S.-G. Li, K.-J. Jiang, M.-J. Su, X.-P. Cui, J.-H. Huang, Q.-Q. Zhang, X.-Q. Zhou, L.-M. Yang, Y.-L. Song, *J. Mater. Chem. A* **2015**, *3*, 9092.

[7] A. T. Barrows, A. J. Pearson, C. K. Kwak, A. D. F. Dunbar, A. R. Buckley, D. G. Lidzey, *Energy Environ. Sci.* **2014**, *7*, 2944.

[8] C. R. Kagan, D. B. Mitzi, C. D. Dimitrakopoulos, *Science* **1999**, *286*, 945.

[9] Z.-K. Tan, R. S. Moghaddam, M. L. Lai, P. Docampo, R. Higler, F. Deschler, M. Price, A. Sadhanala, L. M. Pazos, D. Credgington, F. Hanusch, T. Bein, H. J. Snaith, R. H. Friend, *Nat. Nanotechnol.* **2014**, *9*, 687.

[10] L. Dou, Y. (Micheal) Yang, J. You, Z. Hong, W.-H. Chang, G. Li, Y. Yang, *Nat. Commun.* **2014**, *5*, 5404.

[11] Y. Fang, Q. Dong, Y. Shao, Y. Yuan, J. Huang, *Nat. Photonics* **2015**, *9*, 679.

[12] M. Liu, M. B. Johnston, H. J. Snaith, *Nature* **2013**, *501*, 395.

[13] C.-Y. Chang, C.-Y. Chu, Y.-C. Huang, C.-W. Huang, S.-Y. Chang, C.-A. Chen, C.-Y. Chao, W.-F. Su, *ACS Appl. Mater. Interfaces* **2015**, *7*, 4955.

[14] C.-C. Chen, S.-H. Bae, W.-H. Chang, Z. Hong, G. Li, Q. Chen, H. Zhou, Y. Yang, *Mater. Horiz.* **2015**, *2*, 203.

[15] J. Xu, A. Buin, A. H. Ip, W. Li, O. Voznyy, R. Comin, M. Yuan, S. Jeon, Z. Ning, J. J. McDowell, P. Kanjanaboos, J.-P. Sun, X. Lan, L. N. Quan, D. H. Kim, I. G. Hill, P. Maksymovych, E. H. Sargent, *Nat. Commun.* **2015**, *6*, 7081.

[16] J. T.-W. Wang, Z. Wang, S. Pathak, W. Zhang, D. W. DeQuilettes, F. Wisnivesky-Rocca-Rivarola, J. Huang, P. K. Nayak, J. B. Patel, H. A. Mohd Yusof, Y. Vaynzof, R. Zhu, I. Ramirez, J. Zhang, C. Ducati, C. Grovenor, M. B. Johnston, D. S. Ginger, R. J. Nicholas, H. J. Snaith, *Energy Environ. Sci.* **2016**, *9*, 2892.

[17] X. Gong, M. Li, X.-B. Shi, H. Ma, Z.-K. Wang, L.-S. Liao, *Adv. Funct. Mater.* **2015**, *25*, 6671.

[18] G. E. Eperon, S. D. Stranks, C. Menelaou, M. B. Johnston, L. M. Herz, H. J. Snaith, *Energy Environ. Sci.* **2014**, *7*, 982.

[19] W. Zhang, S. Pathak, N. Sakai, T. Stergiopoulos, P. K. Nayak, N. K. Noel, A. A. Haghighirad, V. M. Burlakov, D. W. deQuilettes, A. Sadhanala, W. Li, L. Wang, D. S. Ginger, R. H. Friend, H. J. Snaith, *Nat. Commun.* **2015**, *6*, 10030.

[20] X. Li, M. I. Dar, C. Yi, J. Luo, M. Tschumi, S. M. Zakeeruddin, M. K. Nazeeruddin, H. Han, M. Grätzel, *Nat. Chem.* **2015**, *7*, 703.

[21] C. M. M. Soe, C. C. Stoumpos, B. Harutyunyan, E. F. Manley, L. X. Chen, M. J. Bedzyk, T. J. Marks, M. G. Kanatzidis, *ChemSusChem* **2016**, *9*, 2656.

[22] J. Pan, C. Mu, Q. Li, W. Li, D. Ma, D. Xu, *Adv. Mater.* **2016**, *28*, 8309.

[23] F. Wang, H. Yu, H. Xu, N. Zhao, *Adv. Funct. Mater.* **2015**, *25*, 1120.

[24] P. K. Nayak, D. T. Moore, B. Wenger, S. Nayak, A. A. Haghighirad, A. Fineberg, N. K. Noel, O. G. Reid, G. Rumbles, P. Kukura, K. A. Vincent, H. J. Snaith, *Nat. Commun.* **2016**, *7*, 13303.

[25] K. Yan, M. Long, T. Zhang, Z. Wei, H. Chen, S. Yang, J. Xu, *J. Am. Chem. Soc.* **2015**, *137*, 4460.

[26] D. P. McMeekin, G. Sadoughi, W. Rehman, G. E. Eperon, M. Saliba, M. T. Hörantner, A. Haghighirad, N. Sakai, L. Korte, B. Rech, M. B. Johnston, L. M. Herz, H. J. Snaith, *Science* **2016**, *351*, 151.

[27] Z. Li, M. Yang, J.-S. Park, S.-H. Wei, J. J. Berry, K. Zhu, *Chem. Mater.* **2016**, *28*, 284.

[28] C. Yi, J. Luo, S. Meloni, A. Boziki, N. Ashari-Astani, C. Grätzel, S. M. Zakeeruddin, U. Rothlisberger, M. Grätzel, *Energy Environ. Sci.* **2015**, *9*, 656.

[29] J.-W. Lee, D.-H. Kim, H.-S. Kim, S.-W. Seo, S. M. Cho, N.-G. Park, *Adv. Energy Mater.* **2015**, *5*, 1501310.

[30] G. E. Eperon, G. M. Paternò, R. J. Sutton, A. Zampetti, A. A. Haghighirad, F. Cacialli, H. J. Snaith, *J. Mater. Chem. A* **2015**, *3*, 19688.

[31] Q. Wang, B. Chen, Y. Liu, Y. Deng, Y. Bai, Q. Dong, J. Huang, *Energy Environ. Sci.* **2017**, *10*, 516.

[32] Z. Wang, D. P. McMeekin, N. Sakai, S. van Reenen, K. Wojciechowski, J. B. Patel, M. B. Johnston, H. J. Snaith, *Adv. Mater.* **2017**, *29*, 1604186.

[33] D. Bi, C. Yi, J. Luo, J.-D. Décoppet, F. Zhang, S. M. Zakeeruddin, X. Li, A. Hagfeldt, M. Grätzel, *Nat. Energy* **2016**, *1*, 16142.

[34] J. W. Mullin, *Crystallization*, Butterworth-Heinemann, Amsterdam, The Netherlands **2001**.

[35] C. Bi, Q. Wang, Y. Shao, Y. Yuan, Z. Xiao, J. Huang, J. Burschka, M. Liu, M. B. Johnston, H. J. Snaith, J.-H. Im, Y. Shao, Z. Xiao, M. A. Green, A. Ho-Baillie, H. J. Snaith, O. Malinkiewicz, H. Zhou, M. M. Lee, Z. Xiao, A. Kojima, K. Teshima, Y. Shirai, T. Miyasaka, Z. Xiao, Q. Chen, Q. Dong, D. Zhao, G. E. Eperon, B. Conings, L. Wang, Q. Chen, N. K. Noel, N. J. Jeon, C. Bi, Q. Wang, Z. Xiao, K.-G. Lim, Y. Fang, I. Mora-Seró, *Nat. Commun.* **2015**, *6*, 7747.

[36] R. Hidalgo-Álvarez, *Structure and Functional Properties of Colloidal Systems*, CRC Press, Boca Raton, FL, USA **2010**.

[37] J. C. Fisher, J. H. Hollomon, D. Turnbull, *J. Appl. Phys.* **1948**, *19*, 775.

[38] N. T. K. Thanh, N. Maclean, S. Mahiddine, *Chem. Rev.* **2014**, *114*, 7610.

[39] I. Robinson, R. Harder, *Nat. Mater.* **2009**, *8*, 291.

[40] A. Pramanick, X. P. Wang, C. Hoffmann, S. O. Diallo, M. R. V. Jørgensen, X.-L. Wang, *Phys. Rev. B* **2015**, *92*, 174103.

[41] G. Williamson, W. Hall, *Acta Metall.* **1953**, *1*, 22.

[42] Y. Zhao, J. Zhang, *J. Appl. Crystallogr.* **2008**, *41*, 1095.

[43] X. Zheng, C. Wu, S. K. Jha, Z. Li, K. Zhu, S. Priya, *ACS Energy Lett.* **2016**, *1*, 1014.

[44] Z. Yang, A. Rajagopal, S. B. Jo, C.-C. Chueh, S. Williams, C.-C. Huang, J. K. Katahara, H. W. Hillhouse, A. K.-Y. Jen, *Nano Lett.* **2016**, *16*, 7739.

[45] K. Wojciechowski, I. Ramirez, T. Gorisse, O. Dautel, R. Dasari, N. Sakai, J. M. Hardigree, S. Song, S. Marder, M. Riede, G. Wantz, H. J. Snaith, *ACS Energy Lett.* **2016**, *1*, 648.

[46] N. Deb, R. R. Dasari, K. Moudgil, J. L. Hernandez, S. R. Marder, Y. Sun, A. Karim, D. G. Bucknall, *J. Mater. Chem. A* **2015**, *3*, 21856.

1607039 (8 of 8)